nature nanotechnology

Article

https://doi.org/10.1038/s41565-023-01376-5

Switchable moiré potentials in ferroelectric WTe₂/WSe₂ superlattices

Received: 11 September 2022

Accepted: 17 March 2023

Published online: 27 April 2023



Kaifei Kang **®** ¹, Wenjin Zhao **®** ², Yihang Zeng³, Kenji Watanabe **®** ⁴, Takashi Taniguchi **®** ⁴, Jie Shan **®** ¹,2.3 ⋈ & Kin Fai Mak **®** ¹,2.3 ⋈

Moiré materials with superlattice periodicity many times the atomic length scale have shown strong electronic correlations and band topology with unprecedented tunability. Non-volatile control of the moiré potentials could allow on-demand switching of superlattice effects but has remained challenging to achieve. Here we demonstrate the switching of the correlated and moiré band insulating states, and the associated nonlinear anomalous Hall effect, by the ferroelectric effect. This is achieved in a ferroelectric WTe₂ bilayer of the T_d structure with a centred-rectangular moiré superlattice induced by interfacing with a WSe₂ monolayer of the H structure. The results can be understood in terms of polarization-dependent charge transfer between two WTe₂ monolayers, in which the interfacial layer has a much stronger moiré potential depth; ferroelectric switching thus turns on and off the moiré insulating states. Our study demonstrates the potential for creating new functional moiré materials by incorporating intrinsic symmetry-breaking orders.

Two-dimensional ferroelectric materials have attracted much recent interest due to their potential in non-volatile memory device applications 1 . In addition to atomically thin ferroelectrics $^{2\text{--}7}$, such as SnTe, CuInP $_2S_6$ and T_d -WTe $_2$, ferroelectricity has also been realized in moiré heterostructures $^{8\text{--}13}$, enabling non-volatile control of correlated electronic states and superconductivity. However, non-volatile electrical switching of the moiré trapping potential for electrons and the associated superlattice effects remains a challenge. Here we achieve this goal by utilizing the intrinsic ferroelectricity in angle-aligned bilayer T_d -WTe $_2$ /monolayer H-WSe $_2$ moiré heterostructures.

Monolayer WTe₂ of the T_d crystal structure consists of a layer of tungsten atoms between two layers of tellurium atoms in a distorted octahedral coordination¹⁴. The structure is centrosymmetric with a mirror line along the crystal *b* axis. At charge neutrality, the material is a quantum spin Hall insulator^{15–17}. Bilayer T_d-WTe₂ comprises two antiparallel monolayers; the structure becomes non-centrosymmetric with a polar axis¹⁸ (inclined from the out-of-plane direction). The presence of the polar axis stabilizes ferroelectricity⁴ and generates Berry curvature dipoles in the momentum space¹⁹ responsible for the nonlinear

anomalous Hall effect (NAHE) $^{20-22}$. Bilayer T_d -WTe $_2$ is a topologically trivial insulator. Figure 1c illustrates its schematic band structure with a flat valence band centred at the Γ point of the Brillouin zone and dispersive conduction bands away from the Γ point 23,24 . The bands are layer-polarized by spontaneous out-of-plane electric polarization.

Ferroelectric moiré heterostructure

We introduce moiré potentials to bilayer WTe₂ by adding a WSe₂ monolayer on it^{25,26} (Fig. 1a). The WSe₂ monolayer is of the H crystal structure, in which the tungsten atoms are between the selenium atoms in the trigonal prismatic coordination. The zigzag crystal axis of WSe₂ is aligned to the crystal a axis of WTe₂. A nearly centred-rectangular moiré superlattice is expected with periods 6.9 nm and 6.4 nm along the a and b axes of WTe₂, respectively. These values are estimated from the lattice mismatch between the two materials (5% and 9%) along the two axes. The corresponding moiré density, $n_{\rm M}$, is about 4.5 × 10¹² cm⁻². These estimates agree with the experimental moiré pattern of a typical aligned WTe₂/WSe₂ heterostructure obtained by piezoresponse force microscopy (PFM) (Fig. 1b; see Methods and Extended Data Fig. 1 for

¹School of Applied and Engineering Physics, Cornell University, Ithaca, NY, USA. ²Kavli Institute at Cornell for Nanoscale Science, Cornell University, Ithaca, NY, USA. ³Laboratory of Atomic and Solid State Physics, Cornell University, Ithaca, NY, USA. ⁴National Institute for Materials Science, Tsukuba, Japan. E-mail: jie.shan@cornell.edu; kinfai.mak@cornell.edu

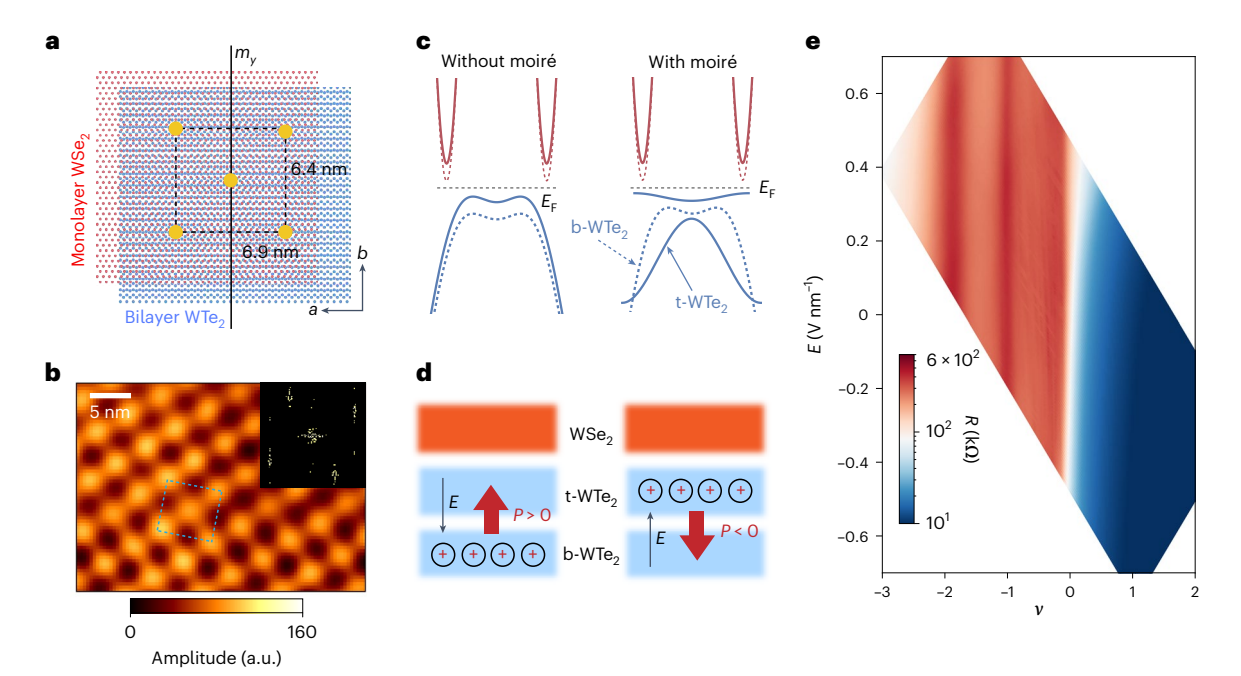


Fig. 1| Bilayer T_d -WTe₂/monolayer H-WSe₂ moiré heterostructure. a, Moiré superlattice for angle-aligned bilayer T_d -WTe₂/monolayer H-WSe₂ heterostructure. Only the tungsten atoms are shown. Yellow dots denote the high-symmetry MM (tungsten on tungsten) sites, which form a centred-rectangular lattice with lattice constants of 6.9 nm along the crystal a axis of WTe₂ and 6.4 nm along the crystal b axis of WTe₂ (m_y is the mirror line). The dashed rectangle marks the moiré unit cell. The black arrows mark the crystal a and b axes of bilayer WTe₂. b, PFM image of a typical moiré heterostructure. The dashed rectangle marks the moiré unit cell. Inset: Fourier transform of the PFM image; there are four diffraction peaks corresponding to the centred-rectangular moiré lattice. c, Schematics for the bilayer WTe₂ band structure with and without

moiré effects. Red and blue curves correspond to conduction and valence bands, respectively. As shown in the right-hand panels, moiré bands are formed only on the top WTe_2 (t- WTe_2) layer (solid blue curves). The bottom WTe_2 (b- WTe_2) layer experiences substantially weaker moiré potential; the bands are dispersive (dashed curves). The horizontal grey dashed line denotes the Fermi level. \mathbf{d} , Polarization-dependent hole (red cross) distributions in bilayer WTe_2 . P and E are, respectively, the spontaneous polarization and its corresponding internal electric field. \mathbf{e} , Electric-field and filling-factor dependence measured at 30 K for the longitudinal resistance of angle-aligned monolayer T_d - WTe_2 /monolayer WTe_2 , heterostructure.

details). The two lattice vectors form an angle of about 84° . The moiré lattice is robust and insensitive to twist-angle variations in the sample as a result of the large lattice mismatch. The nearly centred-rectangular lattice also contrasts with the triangular and honeycomb moiré lattices examined by most existing studies to date^{27–31}.

The heterostructure has a type I band alignment with both the conduction band minimum and valence band maximum from bilayer WTe $_2$ (ref. 32). The WSe $_2$ layer remains charge-neutral at all times; it only provides a moiré potential responsible for the flat bands in the WTe $_2$ layer. Figure 1c shows the schematic band structure, including the zone-folding effect on the bilayer WTe $_2$ bands 20 . The top WTe $_2$ layer directly interfacing with WSe $_2$ is expected to experience a substantially stronger moiré potential than the bottom WTe $_2$ layer; the moiré bands for the top layer are expected to be much flatter. Such layer-sensitive moiré effects in bilayer WTe $_2$, combined with its intrinsic ferroelectric order, form the basis for ferroelectric control of the moiré potential in this study.

Below we demonstrate the effects of ferroelectric switching on the correlated insulating states and the Berry curvature dipole distribution in the correlated flat bands. The heterostructure is encapsulated between top and bottom boron nitride and graphite gates for independent controls of the charge carrier density ν (in units of $n_{\rm M}$) and the electric field E perpendicular to the sample plane (positive field defined as pointing from WTe₂ to WSe₂). See Methods for details on device fabrications, calibration of moiré density and measurements.

Switchable moiré potential by ferroelectricity

To contrast the behaviour of bilayer WTe₂ devices, we first examine the density- and electric-field-dependent transport properties in

an angle-aligned monolayer WTe₂/monolayer WSe₂ heterostructure (Fig. 1e). Because monolayer WTe₂ is a quantum spin Hall insulator ¹⁵⁻¹⁷, we fabricate an edge-avoiding device to access the bulk resistivity of the material (Methods and Extended Data Fig. 2). We only perform measurements down to 30 K because the sample resistance increases substantially below this temperature. In Fig. 1e, we observe resistance peaks at filling factors of v = 0, -1, -2. They correspond to the band insulating state when WTe₂ is at charge neutrality ($\nu = 0$), the moiré band insulating state when the first moiré valence band is fully filled with holes ($\nu = -2$), and the correlated insulating state (probably a Mott insulator) for a half-filled moiré band ($\nu = -1$). The insulating states at v = -1, -2 confirm the formation of flat moiré valence bands in monolayer WTe₂ (see Extended Data Fig. 3 for results on other devices). In contrast, no insulating state is observed at v = 1, 2 on the electron doping side (see also Figs. 2 and 3). The result demonstrates the substantially weaker moiré effects on the conduction bands, possibly due to the small conduction band mass (~1/3 of the valence band mass) in WTe₂ (refs. 20,24,33) and the small moiré periods in the WTe₂/WSe₂ heterostructure. Moreover, all observed insulating states show weak and non-hysteretic electric field dependence, consistent with the absence of ferroelectricity in monolayer WTe₂ (ref. 4).

Next, we examine the density- and electric-field-dependent resistance in a bilayer WTe₂ device under forward (from negative to positive) and backward (from positive to negative) scans of the electric field in Fig. 2a,b, respectively. The edge-avoiding geometry is no longer needed because bilayer WTe₂ is a topologically trivial insulator 23,24 . Lower-temperature measurements are also possible. Similar to the monolayer device, we observe insulating states at $\nu=-1$, -2 for hole doping, a charge-neutral insulating state at $\nu=0$, and no

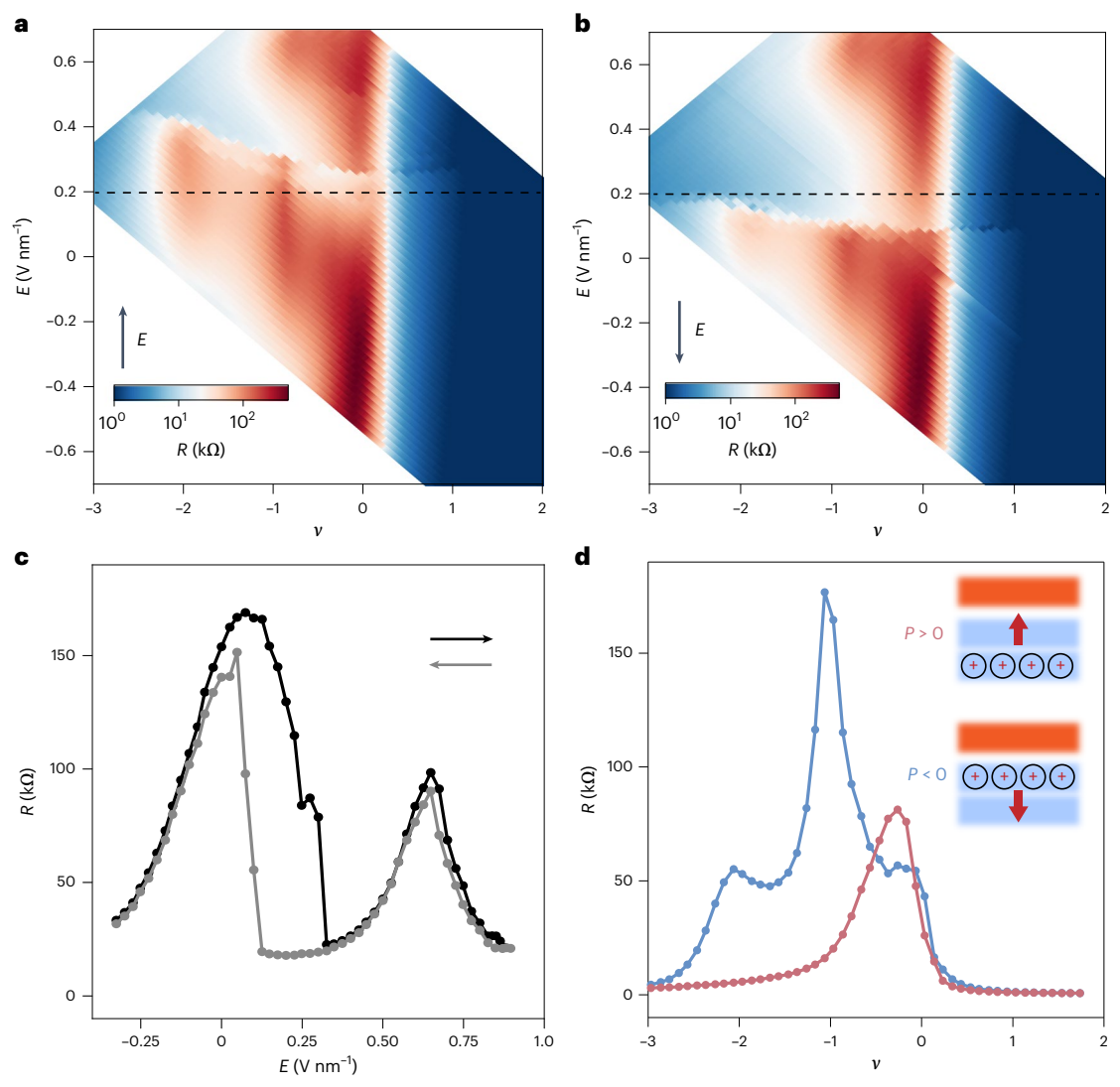


Fig. 2 | Switching moiré potential by ferroelectricity. a,b, Electric-field and filling-factor dependence for the longitudinal resistance of an angle-aligned bilayer T_d -WTe₂/monolayer H-WSe₂ heterostructure at 10 K. The black arrows label the forward (a) and backward (b) electric field scan directions. Hysteretic electric-field dependence corresponding to ferroelectric switching is observed.

c, Electric-field dependence of the longitudinal resistance at $\nu = -1$. The arrows mark the field scan directions. **d**, Filling-factor-dependent longitudinal resistance extracted from **a** (blue) and **b** (red) at $E = 0.2 \,\mathrm{V}$ nm⁻¹ (the black dashed lines in **a** and **b**). They denote the two spontaneous polarization states P > 0 and P < 0 (inset). Moiré insulating states are observed only for P < 0.

moiré insulating states for electron doping. However, unlike the monolayer device, strong electric-field dependence is observed. In particular, robust insulating states at v = -1, -2 are observed mainly for $E \lesssim 0.3 \,\mathrm{V \, nm^{-1}}$ in the forward scan (Fig. 2a) and for $E \lesssim 0.1 \,\mathrm{V \, nm^{-1}}$ in the backward scan (Fig. 2b). A sharp resistance jump and an electric-field hysteresis are also observed near these critical fields, as exemplified by the electric-field-dependent resistance at v = -1 in Fig. 2c (similar data at other filling factors are shown in Extended Data Fig. 4). (The extra resistance step near $E = 0.25 \text{ V nm}^{-1}$ is probably caused by the formation and propagation of ferroelectric domains in the bilayer WTe₂ (refs. 6,34,35).) In addition to the hysteresis, a non-monotonic electric field dependence is also observed (the origin is discussed in Methods). The results demonstrate the effects of ferroelectric switching (in bilayer WTe₂) on the moiré physics. The centre of the ferroelectric switching is shifted from 0 V nm⁻¹ to ~0.2 V nm⁻¹ and disperses with hole doping because of the built-in electric field in the asymmetric heterostructure $(WSe_2 is on top of WTe_2)$.

We further illustrate the effects of ferroelectric switching by plotting the density-dependent resistance near the centre of the hysteresis (at fixed $E=0.2~\rm V~nm^{-1}$) for both forward and backward field scans (Fig. 2d). The two cases represent the two remnant states of spontaneous polarization P in the ferroelectric WTe₂: positive polarization (P>0, pointing from WTe₂ to WSe₂) for backward scan and negative polarization (P<0, pointing from WSe₂ to WTe₂) for the forward scan. Insulating states at v=-1, -2 associated with the moiré valence band are observed only for P<0; only the v=0 insulating state remains for P>0. The charge neutrality point is also nearly independent of the sign of P, showing the negligible change in the total doping density by ferroelectric switching.

The results above can be understood based on the interlayer transfer of mobile holes in bilayer WTe₂ driven by its spontaneous ferroelectric polarization, which originates from the electric-field-switchable ionic displacements in the material 6,36 . When positive polarization (P > 0) is prepared, the internal electric field from the displaced ions (or bound charges) within the bilayer WTe₂ is negative; the field splits the electronic bands of the top and bottom WTe₂ layer via the Stark effect and pushes the mobile holes to the bottom layer (Fig. 1d). The reverse happens when negative polarization (P < 0) is prepared (Fig. 1d).

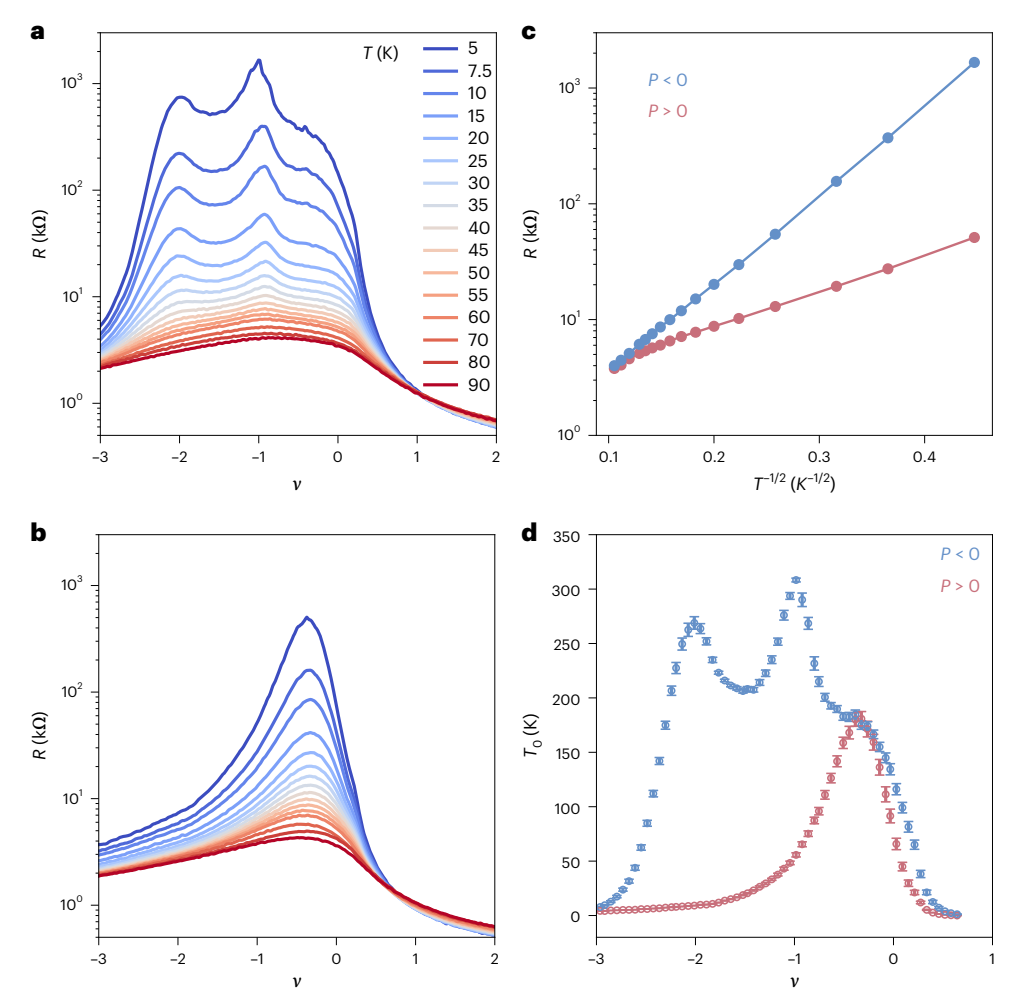


Fig. 3 | **Temperature-dependent electrical transport. a,b**, Filling-factor-dependent longitudinal resistance at varying temperatures from 5 K to 90 K for P < 0 (**a**) and P > 0 (**b**). Insulating-like behaviour is observed for the entire hole-doping region in both **c**ases. **c**, Resistance (log scale) versus $\mathcal{T}^{-1/2}$ at v = -1 for both P < 0 and P > 0. The linear dependence demonstrates Efros–Shklovskii variable-

range hopping. **d**, Filling-factor dependence of the extracted temperature T_0 for both P < 0 and P > 0. Enhancements at the moiré insulating states are observed, showing the shortened localization lengths for P < 0. Error bars denote the standard deviations from fitting the data in **c** (N = 16 data points have been used).

Because holes in the top layer interfacing directly with the WSe₂ layer experience a strong moiré potential, robust insulating states at $\nu = -1$, -2 are observed for P < 0. Conversely, the absence of these insulating states for P > 0 shows the substantially weaker moiré potential in the bottom WTe₂ layer.

Note that the total electric polarization is a sum of both the bound charge and mobile hole contributions; the two contributions point in opposite directions. The bound charge contribution dominates the entire hole doping range; this guarantees nearly complete (that is, 100%) interlayer hole transfer upon ferroelectric switching and the emergence of the moiré insulating states at v = -1, -2 for P < 0. Otherwise, the more mobile holes in the bottom layer would electrically shunt the bilayer conduction irrespective of the sign of P; moiré insulating states would not have been observed.

Variable-range hopping transport

To gain further insights into how ferroelectric switching influences the charge transport in bilayer WTe₂, we perform temperature-dependence studies for both P < 0 and P > 0, which correspond to with and without moiré effects, respectively. Figure 3a,b shows the density-dependent resistance at varying temperatures (5–90 K) for the two states. Metallic transport (decreasing resistance with decreasing temperature)

is observed only on the electron doping side, where moiré physics is not observable; a metal-insulator transition is also observed near v=0.7. The material exhibits insulator-like behaviour for the entire hole-doping range (increasing resistance with decreasing temperature), even when there is no moiré physics for P>0. The v=-1, -2 insulating states for P<0 survive up to about 70 K while the ferroelectricity persists to near room temperature.

The temperature-dependent resistance at v=-1 for both P<0 and P>0 is shown in Fig. 3c (similar dependence at other densities is shown in Extended Data Fig. 5). For temperatures below about 100 K, the resistance R scales with the temperature T according to the Efros-Shklovskii variable-range hopping model 37,38 , $R \propto \exp(T_0/T)^{1/2}$, for over two orders of magnitude in R. The characteristic temperature $T_0=\frac{2.8\,e^2}{4\pi\varepsilon\varepsilon_0k_B\xi}$ is inversely proportional to the localization length ξ

of holes in the bilayer WTe₂ (here e, ε_0 , ε and k_B denote the electron charge, the vacuum permittivity, the dielectric constant of the substrate and the Boltzmann constant, respectively). The density dependence of T_0 is extracted in Fig. 3d. The temperature T_0 is substantially enhanced over the entire hole-doping range for P < 0; additional enhancement at the v = -1, -2 insulating states is also observed. The results demonstrate the additional localization of holes

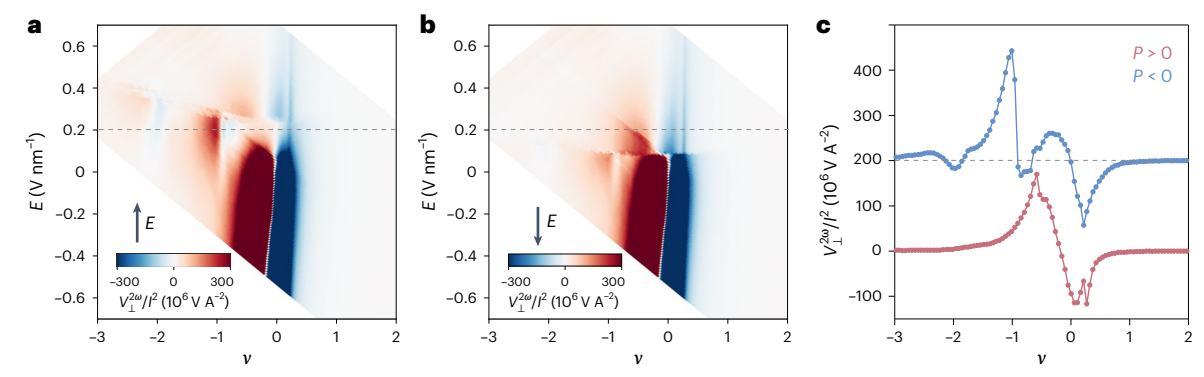


Fig. 4 | **Switching the nonlinear anomalous Hall transport by ferroelectricity. a,b,** Electric-field- and filling-factor-dependent nonlinear anomalous Hall response $V_{1}^{2\omega}/l^2$ at 30 K for the forward (**a**) and backward (**b**) electric field scan directions (black arrows). Hysteretic electric-field dependence corresponding to ferroelectric switching is observed. **c,** Filling-factor-dependent $V_{1}^{2\omega}/l^2$ for P < 0

and P>0 extracted from **a** (blue) and **b** (red), respectively, at $E=0.2 \, \mathrm{V \, mm^{-1}}$ (the black dashed lines in **a** and **b**). The two curves are vertically displaced for clarity. The horizontal dashed line marks $V_{\perp}^{2\omega}/f^2=0$ for P<0. Nonlinear anomalous Hall resets are observed at the moiré insulating states at $\nu=-1$, -2 only for P<0.

that shortens ξ (\approx 35 nm for T_0 = 300 K) when the moiré potential becomes stronger for P < 0.

Switchable NAHE

Finally, we examine the effects of ferroelectric switching on the topological transport properties. The presence of an in-plane polar axis (along the mirror line of WTe₂) in the non-centrosymmetric centred-rectangular moiré lattice allows the generation of an out-of-plane magnetization under a bias current perpendicular to the mirror line^{19,21}. The current-induced magnetization can in turn induce an anomalous Hall effect probed by the same bias current. The anomalous Hall voltage thus scales with the bias current squared, giving rise to an NAHE^{19–22}. The effect provides a powerful probe of the Berry curvature dipoles (an imbalance in the Berry curvature occupations) in moiré materials^{39,40}.

To measure the NAHE in the WTe₂/WSe₂ moiré heterostructure, we bias an a.c. current (1) perpendicular to the mirror line of the moiré lattice and simultaneously measure the first-harmonic longitudinal voltage (V_{\parallel}) and the second-harmonic transverse voltage $(V_{\perp}^{2\omega})$ (Methods). Figure 4a,b shows the density and electric-field dependence of $V_{\perp}^{2\omega}/I^2$ under forward and backward scans in the electric field, respectively. The quantity provides a measure of the nonlinear anomalous Hall response (Extended Data Fig. 6). The measurement temperature is kept above 25 K to avoid large sample resistance. The results correlate with the behaviour for the resistance in Fig. 2a,b. In particular, a strong NAHE with sign reversal in $V_{\perp}^{2\omega}/I^2$ is observed at v = -1, -2 for $E \lesssim 0.3 \,\mathrm{V} \,\mathrm{nm}^{-1}$ in the forward scan and for $E \lesssim 0.1 \,\mathrm{V} \,\mathrm{nm}^{-1}$ in the backward scan; otherwise only the v = 0 region shows a strong NAHE. There is also a sharp jump in $V_{\perp}^{2\omega}/l^2$ and an electric-field hysteresis near these critical electric fields. We extract the density-dependent $V^{2\omega}/I^2$ for the two remnant states of spontaneous polarization P < 0 and $\overline{P} > 0$ in Fig. 4c. (Temperature dependence is shown in Extended Data Fig. 7.) A strong NAHE with sign reversal in $V_{\perp}^{2\omega}/l^2$ is observed at $\nu = 0, -1, -2$ for P < 0; only the characteristic response at v = 0 remains for P > 0.

The results demonstrate the ferroelectric switching of the NAHE. In the absence of the moiré potential (P>0), the Berry curvature and its dipole are concentrated near the WTe₂ conduction and valence band edges. The NAHE is strong near charge neutrality $(\nu=0)$; the sign reversal in $V_{\perp}^{2\omega}/P^2$ reflects the opposite Berry curvature dipoles for the conduction and valence bands^{20,23}. When flat bands are formed due to the moiré potential (P<0), the Berry curvature and its dipole are redistributed within the moiré Brillouin zone⁴¹; the small moiré band gap is expected to enhance the Berry curvature effects substantially^{41,42}. In the strong correlation limit (at which Coulomb repulsion exceeds the

electronic bandwidth), Hubbard bands are formed; Berry curvatures of opposite signs are expected to concentrate near the Hubbard band edges, resulting in the characteristic NAHE response observed at v = -1, -2. Interestingly, the sign reversal in $V_{\perp}^{2\omega}/I^2$ at v = -1, -2 resembles the resets of the Hall density at integer fillings in graphene moiré materials⁴³. The resets reflect the changing carrier type upon doping an insulating state.

In conclusion, we have demonstrated electrical switching of the moiré potential by ferroelectricity in angle-aligned bilayer WTe₂/monolayer WSe₂; the heterostructure forms a centred-rectangular moiré lattice. The emergence of moiré insulating states at integer filling factors is fully controlled by the spontaneous polarization direction. Ferroelectric switching can also redistribute the Berry curvature dipole in the momentum space, giving rise to a strong NAHE at integer fillings of the moiré lattice. Although the experimental results can be qualitatively understood based on the formation of Hubbard bands, the distribution of Berry curvature dipole within the Hubbard bands in the strong correlation limit (versus that within the single-particle moiré bands in the non-interacting limit) is an open question for future studies; understanding the NAHE in the hopping transport regime⁴⁴ (Fig. 3 and Extended Data Fig. 7) also requires further investigations.

Online content

Any methods, additional references, Nature Portfolio reporting summaries, source data, extended data, supplementary information, acknowledgements, peer review information; details of author contributions and competing interests; and statements of data and code availability are available at https://doi.org/10.1038/s41565-023-01376-5.

References

- Qi, L., Ruan, S. C. & Zeng, Y. J. Review on recent developments in 2D ferroelectrics: theories and applications. Adv. Mater. 33, 2005098 (2021).
- 2. Chang, K. et al. Discovery of robust in-plane ferroelectricity in atomic-thick SnTe. *Science* **353**, 274–278 (2016).
- 3. Liu, F. C. et al. Room-temperature ferroelectricity in $CuInP_2S_6$ ultrathin flakes. *Nat. Commun.* **7**, 12357 (2016).
- Fei, Z. Y. et al. Ferroelectric switching of a two-dimensional metal. Nature 560, 336 (2018).
- Li, L. & Wu, M. H. Binary compound bilayer and multilayer with vertical polarizations: two-dimensional ferroelectrics, multiferroics, and nanogenerators. ACS Nano 11, 6382–6388 (2017).

- Yang, Q., Wu, M. H. & Li, J. Origin of two-dimensional vertical ferroelectricity in WTe₂ bilayer and multilayer. *J. Phys. Chem. Lett.* 9, 7160–7164 (2018).
- Ferreira, F., Enaldiev, V. V., Fal'ko, V. I. & Magorrian, S. J. Weak ferroelectric charge transfer in layer-asymmetric bilayers of 2D semiconductors. Sci. Rep. 11, 13422 (2021).
- Zheng, Z. et al. Unconventional ferroelectricity in moire heterostructures. Nature 588, 71–76 (2020).
- Yasuda, K., Wang, X. R., Watanabe, K., Taniguchi, T. & Jarillo-Herrero, P. Stacking-engineered ferroelectricity in bilayer boron nitride. Science 372, 1458 (2021).
- Wang, X. R. et al. Interfacial ferroelectricity in rhombohedralstacked bilayer transition metal dichalcogenides. *Nat. Nanotechnol.* 17, 367 (2022).
- Weston, A. et al. Interfacial ferroelectricity in marginally twisted 2D semiconductors. Nat. Nanotechnol. 17, 390 (2022).
- Stern, M. V. et al. Interfacial ferroelectricity by van der Waals sliding. Science 372, 1462 (2021).
- Liu, Y., Liu, S., Li, B. C., Yoo, W. J. & Hone, J. Identifying the transition order in an artificial ferroelectric van der Waals heterostructure. *Nano. Lett.* 22, 1265–1269 (2022).
- Brown, B. E. Crystal structures of WTe₂ and high-temperature MoTe₂. Acta Crystallogr. 20, 268 (1966).
- Fei, Z. Y. et al. Edge conduction in monolayer WTe₂. Nat. Phys. 13, 677 (2017).
- Wu, S. F. et al. Observation of the quantum spin Hall effect up to 100 kelvin in a monolayer crystal. Science 359, 76–79 (2018).
- Zhao, W. J. et al. Determination of the spin axis in quantum spin hall insulator candidate monolayer WTe₂. Phys. Rev. X 11, 041034 (2021).
- Sakai, H. et al. Critical enhancement of thermopower in a chemically tuned polar semimetal MoTe₂. Sci. Adv. 2, 11 (2016).
- Sodemann, I. & Fu, L. Quantum nonlinear Hall effect induced by Berry curvature dipole in time-reversal invariant materials. *Phys. Rev. Lett.* 115, 216806 (2015).
- Ma, Q. et al. Observation of the nonlinear Hall effect under time-reversal-symmetric conditions. Nature 565, 337 (2019).
- Kang, K. F., Li, T. X., Sohn, E., Shan, J. & Mak, K. F. Nonlinear anomalous Hall effect in few-layer WTe₃. Nat. Mater. 18, 324 (2019).
- Du, Z. Z., Lu, H. Z. & Xie, X. C. Nonlinear Hall effects. Nat. Rev. Phys. 3, 744–752 (2021).
- Xu, S. Y. et al. Electrically switchable Berry curvature dipole in the monolayer topological insulator WTe₂. Nat. Phys. 14, 900 (2018).
- 24. Qian, X. F., Liu, J. W., Fu, L. & Li, J. Quantum spin Hall effect in two-dimensional transition metal dichalcogenides. *Science* **346**, 1344–1347 (2014).
- Chen, Z. S. et al. Tunable electronic structure in twisted WTe₂/WSe₂ heterojunction bilayer. AIP Adv. 12, 045315 (2022).
- Xie, Y. et al. Gate-tunable van der Waals heterostructure based on semimetallic WTe₂ and semiconducting MoTe₂. Appl. Phys. Lett. 118, 133103 (2021).
- Andrei, E. Y. & MacDonald, A. H. Graphene bilayers with a twist. Nat. Mater. 19, 1265–1275 (2020).

- Balents, L., Dean, C. R., Efetov, D. K. & Young, A. F. Superconductivity and strong correlations in moiré flat bands. *Nat. Phys.* 16, 725–733 (2020).
- 29. Mak, K. F. & Shan, J. Semiconductor moiré materials. Nat. Nanotechnol. 17, 686–695 (2022).
- 30. Kennes, D. M. et al. Moiré heterostructures as a condensed-matter quantum simulator. *Nat. Phys.* **17**, 155–163 (2021).
- 31. Andrei, E. Y. et al. The marvels of moiré materials. *Nat. Rev. Mater.* **6**, 201–206 (2021).
- 32. Liu, Y. Y., Stradins, P. & Wei, S. H. Van der Waals metalsemiconductor junction: weak Fermi level pinning enables effective tuning of Schottky barrier. Sci. Adv. 2, 4 (2016).
- 33. Lv, H. Y. et al. Perfect charge compensation in WTe₂ for the extraordinary magnetoresistance: from bulk to monolayer. *Europhys. Lett.* **110**, 37004 (2015).
- 34. Sharma, P. et al. A room-temperature ferroelectric semimetal. *Sci. Adv.* **5**, 7 (2019).
- 35. Enaldiev, V. V., Ferreira, F. & Fal'ko, V. I. A scalable network model for electrically tunable ferroelectric domain structure in twistronic bilayers of two-dimensional semiconductors. *Nano. Lett.* **22**, 1534–1540 (2022).
- 36. Wang, H. & Qian, X. F. Ferroelectric nonlinear anomalous Hall effect in few-layer WTe₂. npj Comput. Mater. **5**, 119 (2019).
- Efros, A. L., Nguyen, V. L. & Shklovskii, B. I. Variable range hopping in doped crystalline semiconductors. Solid State Commun. 32, 851–854 (1979).
- 38. Efros, A. L. & Shklovskii, B. I. Coulomb gap and low-temperature conductivity of disordered systems. *J. Phys. C* **8**, 49–51 (1975).
- 39. Sinha, S. et al. Berry curvature dipole senses topological transition in a moiré superlattice. *Nat. Phys.* **18**, 765 (2022).
- He, P. et al. Graphene moiré superlattices with giant quantum nonlinearity of chiral Bloch electrons. *Nat. Nanotechnol.* 17, 378 (2022).
- 41. Zhang, C. P. et al. Giant nonlinear Hall effect in strained twisted bilayer graphene. *Phys. Rev. B* **106**, LO41111 (2022).
- 42. Xiao, D., Chang, M. C. & Niu, Q. Berry phase effects on electronic properties. *Rev. Mod. Phys.* **82**, 1959–2007 (2010).
- Saito, Y. et al. Isospin Pomeranchuk effect in twisted bilayer graphene. Nature 592, 220–224 (2021).
- 44. Burkov, A. A. & Balents, L. Anomalous Hall effect in ferromagnetic semiconductors in the hopping transport regime. *Phys. Rev. Lett.* **91**, 057202 (2003).

Publisher's note Springer Nature remains neutral with regard to jurisdictional claims in published maps and institutional affiliations.

Springer Nature or its licensor (e.g. a society or other partner) holds exclusive rights to this article under a publishing agreement with the author(s) or other rightsholder(s); author self-archiving of the accepted manuscript version of this article is solely governed by the terms of such publishing agreement and applicable law.

@ The Author(s), under exclusive licence to Springer Nature Limited 2023

Methods

Device fabrication

T_d-WTe₂/H-WSe₂ moiré heterostructures were fabricated using the standard layer-by-layer stacking method⁴⁵. In short, air-sensitive monolaver and bilaver WTe₂ flakes were exfoliated from bulk crystals (HO Graphene) and identified based on their optical contrast on silicon substrates inside a nitrogen-filled glovebox with ~1 ppm of oxygen and H_2O . The a and b axes of the WTe₂ flakes were determined according to the sharp sample edges. Monolayer WSe₂ flakes were exfoliated under ambient conditions. The WSe₂ crystal axes were determined by polarization- and angle-resolved second-harmonic generation spectroscopy⁴⁶. The zigzag axis of WSe₂ was aligned to the crystal a axis of WTe₂ during the stacking process. To complete the devices, we first defined platinum electrodes in the Hall-bar geometry on a hexagonal boron nitride (hBN, 10-20 nm thick)/graphite (2-5 layers, serving as a bottom gate) heterostructure using electron-beam lithography. We then used a polymer stamp consisting of a polycarbonate film on polydimethylsiloxane to sequentially pick up flakes of graphite, hBN (~3-4 nm), a WSe₂ monolayer and a WTe₂ monolayer or bilayer. The finished heterostructure on the stamp was released onto the prepatterned platinum electrodes (directly touching WTe₂) at 180 °C. The polymer stamp was then dissolved in chloroform. To fabricate the edge-avoiding devices, we inserted a thin hBN spacer (~2 nm) between the moiré heterostructure and the platinum electrodes so that the WTe₂ sample edges do not touch the metal electrodes 47,48. See Extended Data Fig. 2 for the device geometry.

Linear and nonlinear electrical measurements

Electrical transport measurements were carried out in an Oxford Teslatron cryostat down to 1.8 K. Both linear and nonlinear electrical measurements were performed using the standard lock-in technique. Specifically, current with a constant amplitude of 0.5 µA and modulation frequency of 17 Hz was biased along the crystal a axis of WTe2. The longitudinal voltage drop at the same frequency (V_{\parallel}) and the Hall voltage drop at the second-harmonic frequency $(V_{\perp}^{2\omega})$ were simultaneously recorded by lock-in amplifiers (Stanford Research SR830). In general, the sample resistance increases substantially at low temperatures; therefore, we limited the nonlinear anomalous Hall measurements to temperatures above 25 K. The nonlinear anomalous Hall response was verified to be independent of the excitation frequency (Extended Data Fig. 6). In addition, we also measured the longitudinal resistance with current biased along the crystal b axis of WTe₂ (Extended Data Fig. 8). The linear transport behaviour is largely independent of the bias current direction.

Due to the large sample resistance at low temperatures and possible excitonic interactions⁴⁹, calibration of the carrier density using the ordinary Hall effect is unreliable. Instead, we calibrate the carrier density (n) and moiré density ($n_{\rm M}$) of the device shown in the main text using the parallel-plate capacitor model: $n = \frac{\varepsilon \varepsilon_0 V_{\rm tg}}{d_{\rm tg}} + \frac{\varepsilon \varepsilon_0 V_{\rm bg}}{d_{\rm bg}}$. Here $d_{\rm tg} \approx 4$ nm and $d_{\rm tg} \approx 22$ nm are the top and bottom hBN gate dielectric thicknesses measured by atomic force microscopy; $V_{\rm tg}$ and $V_{\rm bg}$ are the top and bottom gate voltages; and $\varepsilon \approx 3$ is the hBN dielectric constant. A hole density of $(5.0-5.5) \times 10^{12}$ cm⁻² at v = -1 was obtained using the applied gate voltages relative to those at v = 0; the value is about 10-20% larger than the moiré density $(4.5 \times 10^{12} \ {\rm cm}^{-2})$ estimated using the known lattice parameters (see main text). The discrepancy may arise from the misalignment of the WTe₂ and WSe₂ crystal axes (up to about 2°) and from the identification of the gate voltage corresponding to zero doping density.

PFM

To characterize the moiré pattern using PFM, we fabricated an angle-aligned monolayer T_d -WTe $_2$ /H-WSe $_2$ heterostructure on a polymer stamp consisting of polycarbonate on polydimethylsiloxane. Flakes of hBN, monolayer WTe $_2$ and monolayer WSe $_2$ were sequentially

picked up by the polymer stamp. We then flipped the stamp for the PFM characterization with WSe $_2$ on the top surface to protect WTe $_2$ from oxidation. PFM was performed using a Bruker Veeco Icon atomic force microscope with Oxford Instrument Asylum Research ASYELEC-01 Ti/Ir-coated silicon probes. An a.c. bias voltage with a magnitude of 4 V and frequency of 680 kHz was applied to drive the probe during the scan. To improve the signal-to-noise ratio of the obtained moiré pattern, the raw PFM images were Fourier filtered with a threshold of 72% of the maximum intensity (Extended Data Fig. 1). We further fit the fast Fourier transform satellite peak intensity to a Gaussian function, which gives a standard deviation of -8.8%, corresponding to 1–2° variation in the twist angle. Such twist angle variation is probably exaggerated by the PFM noise, the limited fast Fourier transform resolution and the random buckling of the sample on top of a polymer film.

Estimate of the first moiré valence band bandwidth

The bandwidth of the first moiré valence band $\sim \frac{h^2}{8m^2 a_{\rm M}^2} \approx 17$ meV can be estimated using the WTe₂ effective mass $m^* \approx 0.9 m_0$ (ref. 33). Here h, m_0 and $a_{\rm M} \approx 6.5$ nm denote the Planck's constant, the free electron mass and the moiré period, respectively. The bandwidth is comparable to or even smaller than the existing moiré materials²⁷⁻³¹.

Non-monotonic electric-field-dependent resistance

Extended Data Fig. 4 shows the electric-field-dependent longitudinal resistance for both field scan directions at selected filling factors. We focus our discussions on v = 0 and -1, at which high out-of-plane electric fields can be applied. Non-monotonic electric field dependence of the resistance is observed. In particular, resistance peaks are observed at electric fields $E \approx -0.3 \, \text{V nm}^{-1}$ and $0.55 \, \text{V nm}^{-1}$ for v = 0 and at $E \approx 0.1 \, \text{V nm}^{-1}$ and $0.65 \, \text{V nm}^{-1}$ for v = -1.

To understand the observation, we consider the band structure and interlayer charge distribution in bilayer WTe₂ under an applied electric field E. In the presence of a spontaneous polarization P (dominated by the bound charge contribution), the total electric field is given by $E_{\rm tot} = E - P/\chi \epsilon_0$ (where χ is the electric susceptibility). At $\nu = 0$ (charge neutrality), the resistance reflects the charge gap size of bilayer WTe₂. The gap size is the largest for $E_{\rm tot} = 0$. It decreases linearly with $E_{\rm tot}$ due to the interlayer Stark effect²⁰ (Fig. 1c). The maximum gap size is therefore expected at $E = \pm |P|/\chi \epsilon_0$, which is consistent with the observed resistance peaks at $E \approx -0.32$ V nm⁻¹ and 0.58 V nm⁻¹ in Extended Data Fig. 4. The asymmetry in the observed electric fields is caused by the heterostructure asymmetry, which shifts the centre of the electric-field dependence by about 0.2 V nm⁻¹. Away from these two fields, the gap size decreases with $E_{\rm tot}$, and the resistance decreases.

On the other hand, the resistance at v=-1 is primarily determined by the location of the doped holes, specifically, high (low) resistance for holes residing in the top (bottom) WTe₂ layer. For P < 0, a negative electric field (E < 0) pushes the doped holes away from the WSe₂/WTe₂ interface, thus reducing the moiré effects (Fig. 1d); the resistance decreases monotonically (Extended Data Fig. 4). For P > 0, an electric field $E > 0.4 \text{ V nm}^{-1}$ pushes the doped holes towards the WSe₂/WTe₂ interface, thereby enhancing the moiré effects (Fig. 1d); the resistance increases and peaks at $E \approx 0.65 \text{ V nm}^{-1}$, beyond which the charge gap decreases due to the interlayer Stark effect (as discussed above). Finally, hysteretic switching behaviour is observed for $0 < E < 0.4 \text{ V nm}^{-1}$; the resistance depends on the direction of P. The centre of the ferroelectric switching is shifted by about 0.2 V nm^{-1} because of the heterostructure asymmetry.

Data availability

Source data are provided with this paper. Additional data related to this paper are available from the corresponding authors upon reasonable request. Source data are provided with this paper.

References

- Wang, L. et al. One-dimensional electrical contact to a two-dimensional material. Science 342, 614–617 (2013).
- Tang, Y. H. et al. Simulation of Hubbard model physics in WSe₂/WS₂ moiré superlattices. Nature **579**, 353–358 (2020).
- 47. Zhu, J. C., Li, T. X., Young, A. F., Shan, J. & Mak, K. F. Quantum oscillations in two-dimensional insulators induced by graphite gates. *Phys. Rev. Lett.* **127**, 247702 (2021).
- 48. Wang, P. J. et al. Landau quantization and highly mobile fermions in an insulator. *Nature* **589**, 225–229 (2021); erratum **591**, E17 (2021).
- Jia, Y. Y. et al. Evidence for a monolayer excitonic insulator. Nat. Phys. 18, 87 (2022).

Acknowledgements

We thank A. Rubio, Y. Zhang and J. Zhang for the fruitful discussions. This work was supported by the Air Force Office of Scientific Research MURI under award number FA9550-18-1-0480 (device fabrication), the US Department of Energy (DOE), Office of Science, Basic Energy Sciences (BES), under award number DE-SC0019481 (transport measurements), the Cornell Center for Materials Research through the NSF MRSEC programme under award DMR-1719875 (scanning probe characterization) and the NSF Platform for the Accelerated Realization, Analysis and Discovery of Interface Materials (PARADIM) under cooperative agreement DMR-2039380 (analysis). This work was also funded in part by the Gordon and Betty Moore Foundation. The growth of the hBN crystals was supported by the Elemental Strategy Initiative of MEXT, Japan, and CREST (JPMJCR15F3), JST. This work made use of the Cornell NanoScale Facility, an NNCI member supported by NSF grant

NNCI-2025233. W.Z. acknowledges support from the Kavli Postdoctoral Fellowship.

Author contributions

K.K. fabricated the devices. K.K. and W.Z. performed the electrical measurements. Y.Z. and K.K. performed the PFM measurements. K.K. analysed the data. K.W. and T.T. grew the hBN crystals. K.K., J.S. and K.F.M. designed the scientific objectives, oversaw the project and co-wrote the paper. All authors discussed the results and commented on the paper.

Competing interests

The authors declare no competing interests.

Additional information

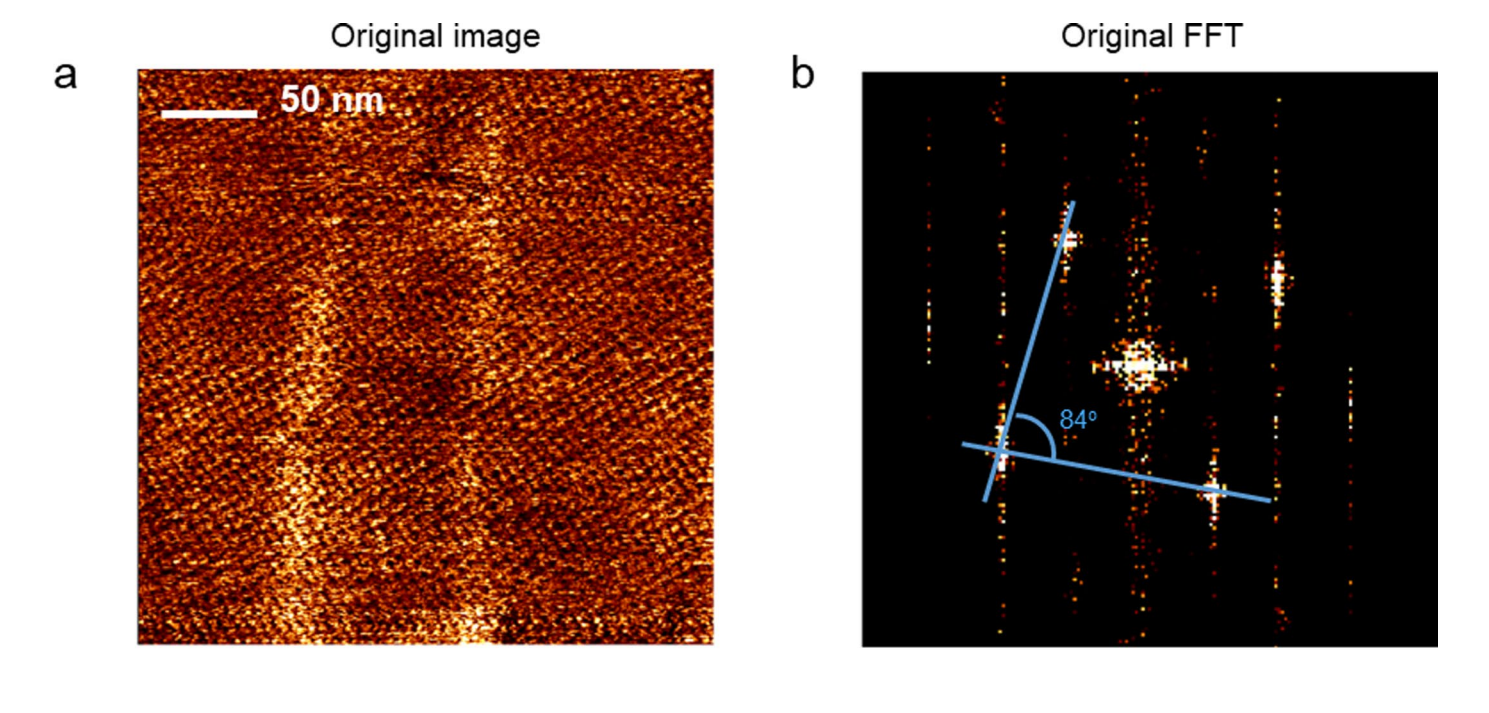
Extended data is available for this paper at https://doi.org/10.1038/s41565-023-01376-5.

Supplementary information The online version contains supplementary material available at https://doi.org/10.1038/s41565-023-01376-5.

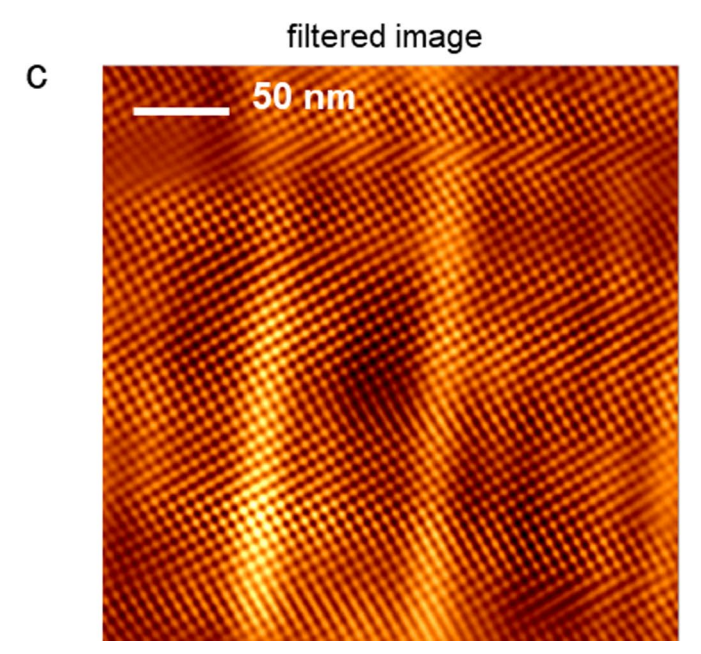
Correspondence and requests for materials should be addressed to Jie Shan or Kin Fai Mak.

Peer review information *Nature Nanotechnology* thanks Menghao Wu, Daniel Rhodes and the other, anonymous, reviewer(s) for their contribution to the peer review of this work.

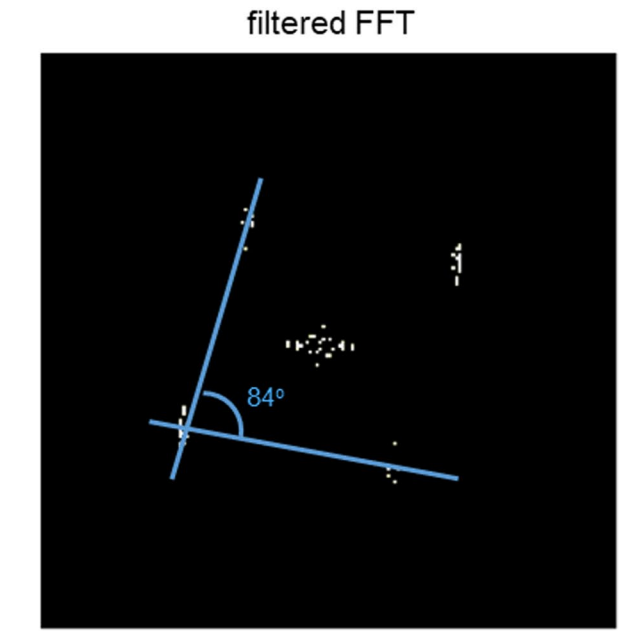
Reprints and permissions information is available at www.nature.com/reprints.



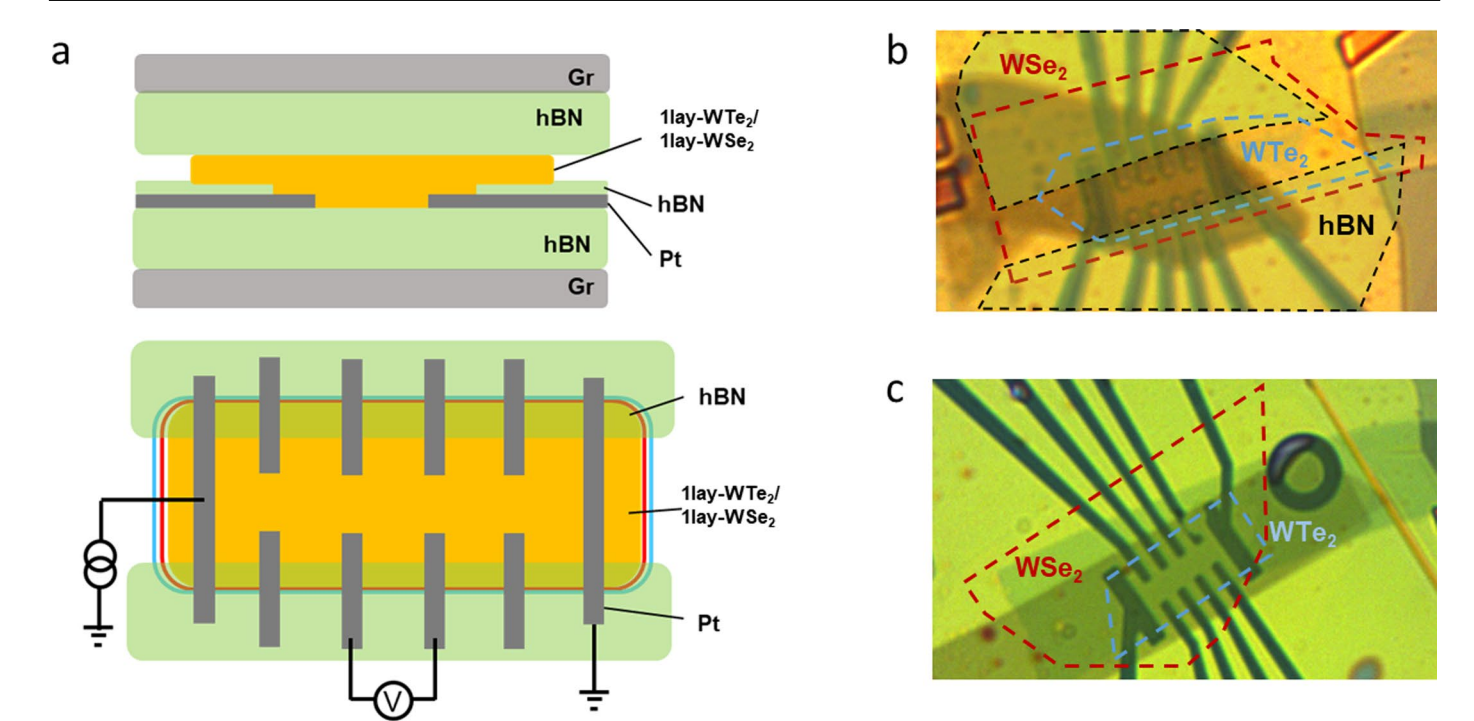
d



Extended Data Fig. 1 | **PFM images and analysis. a**, Raw PFM image of an angle-aligned monolayer T_d -WTe₂/monolayer H-WSe₂ heterostructure. **b**, Fourier transform of the raw image. Fourier peaks corresponding to a

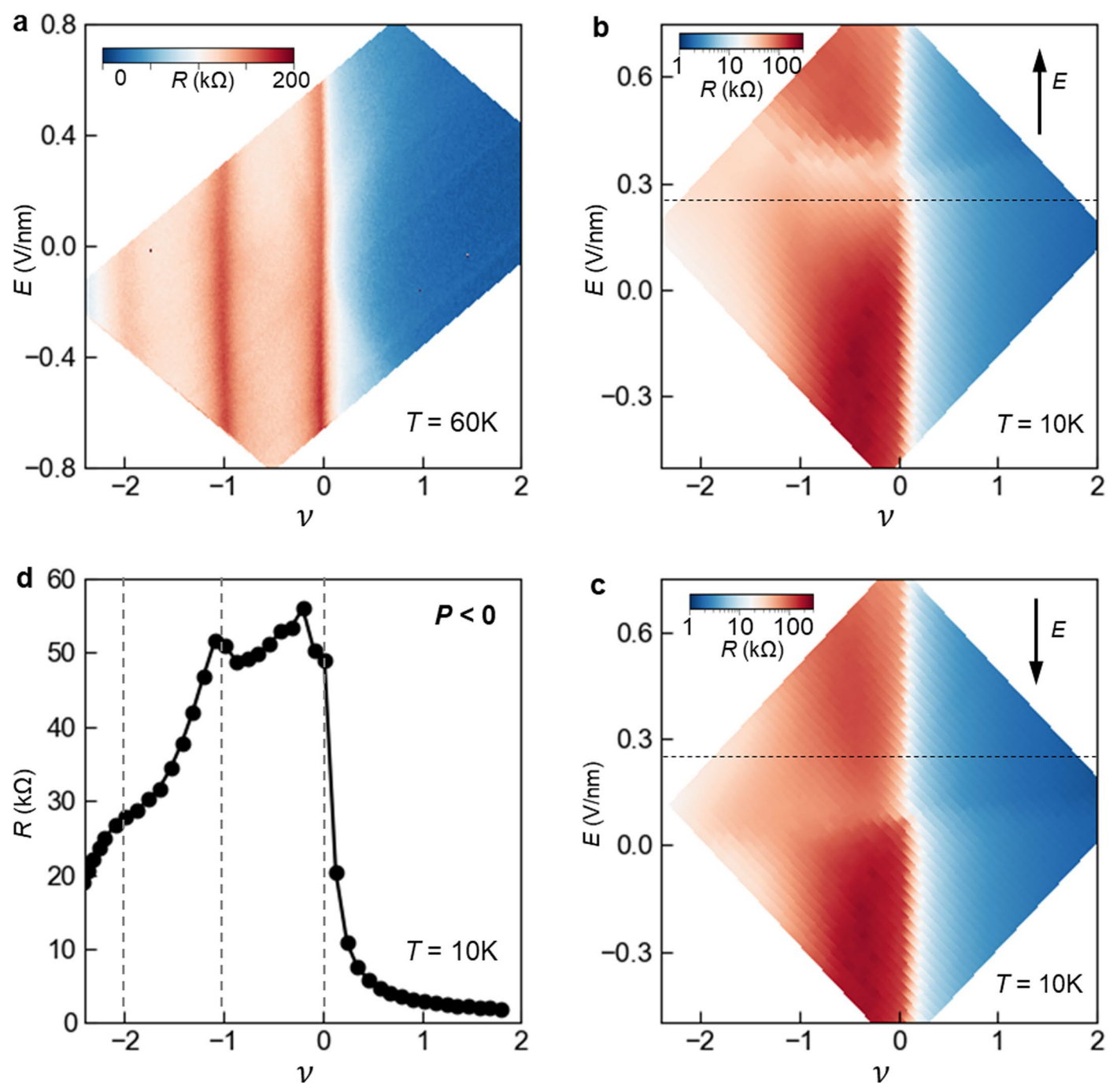


centred-rectangular lattice can be clearly observed. **c**, **d**, The Fourier-filtered PFM image (**c**) and the corresponding Fourier transform (**d**). A high-pass filter is applied with a threshold of 72 % of the maximum intensity.



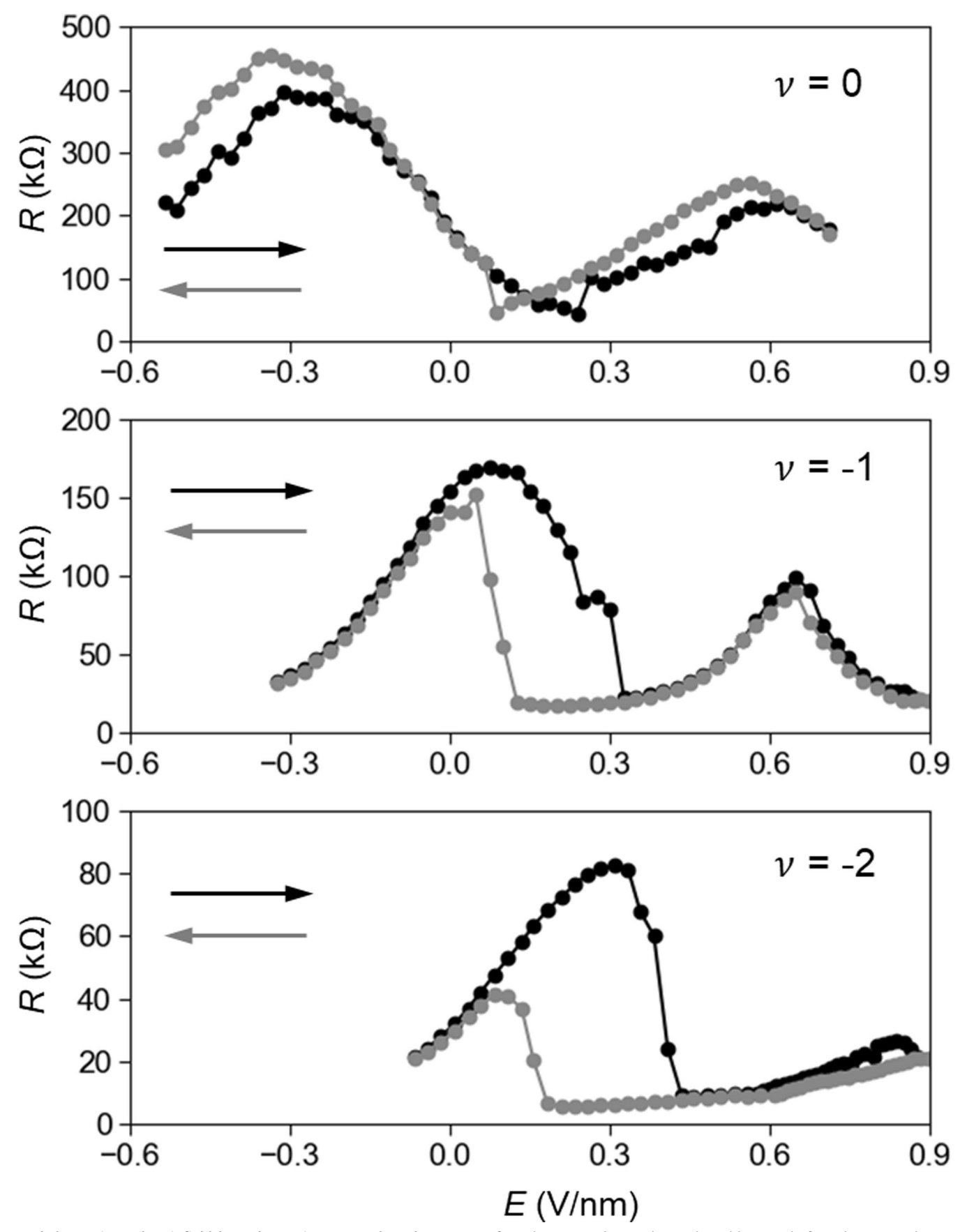
Extended Data Fig. 2 | Device structures for aligned T_d -WTe₂/monolayer H-WSe₂ devices. a, schematics of an angle-aligned monolayer WTe₂/monolayer WSe₂ device. Top: cross-section of the device. A thin hBN spacer is inserted between the WTe₂ and the platinum (Pt) electrodes to avoid direct edge contacts. Gr stands for few-layer graphite gate electrode. Bottom: top view of the device. The blue and red lines denote the helical edge states of a quantum spin Hall

insulator. The measurement configuration is also shown. ${\bf b}$, optical image of a typical angle-aligned monolayer WTe $_2$ / monolayer WSe $_2$ device. Red, blue and black dashed lines mark the WSe $_2$, the WTe $_2$, and the hBN spacer flakes, separately. ${\bf c}$, optical image of the a typical angle-aligned bilayer WTe $_2$ / monolayer WSe $_2$ device. Red and blue dashed lines mark the WSe $_2$ and the bilayer WTe $_2$ flakes, separately.



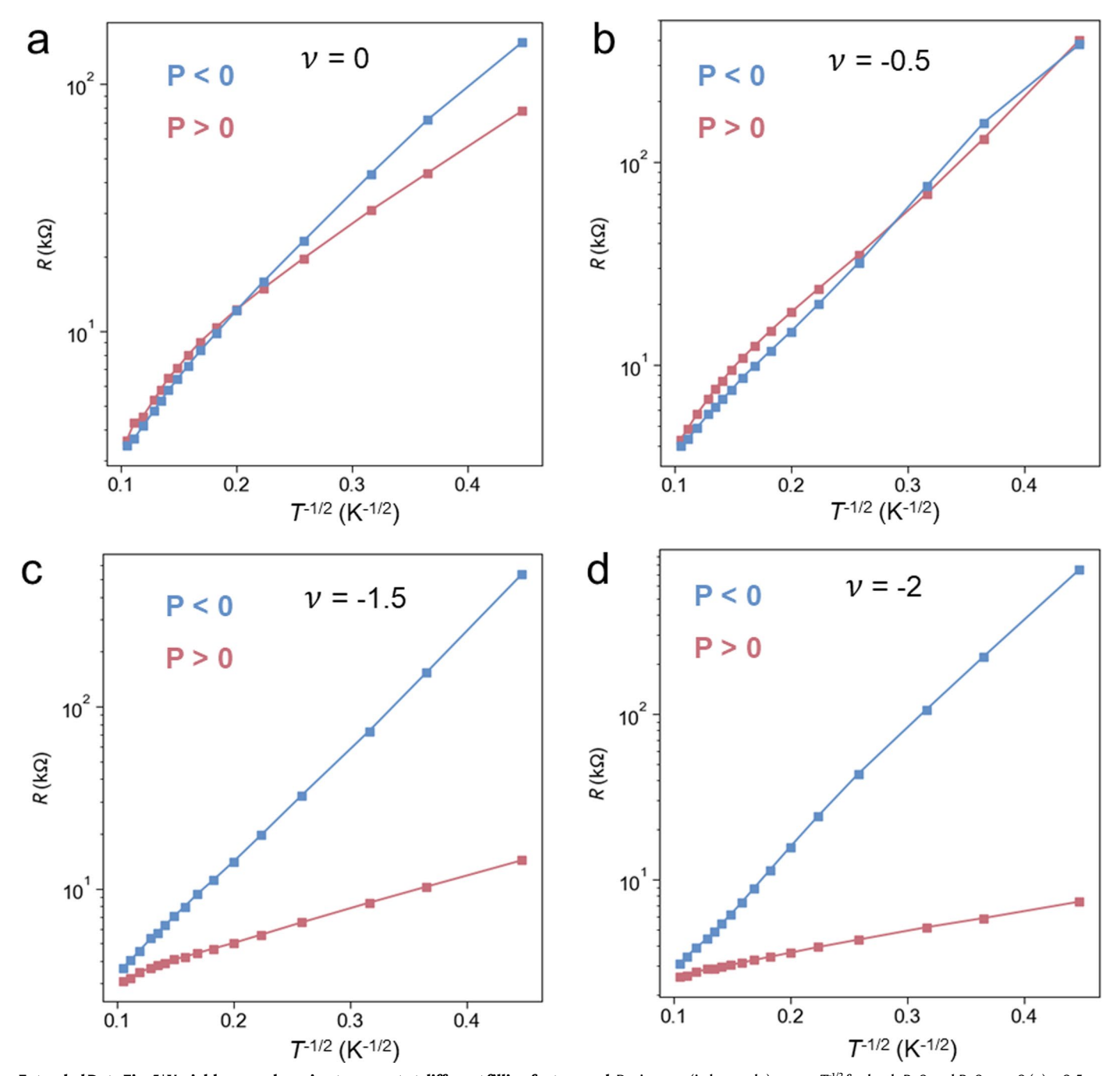
Extended Data Fig. 3 | **Repeatability of the data. a**, Two-terminal sample resistance as a function of filling factor and electric field in another angle-aligned 1lay-WTe $_2$ /1lay-WSe $_2$ moiré device at T = 60 K. **b,c**, Four-terminal sample resistance as a function of filling factor and electric field in another angle-aligned 2lay-WTe $_2$ /1lay-WSe $_2$ moiré device at T = 10 K. Both forward and backward

field scans are shown. **d**, Filling factor dependence of the sample resistance at $E = -0.25 \, \text{V/nm}$ for P < 0. The moiré insulating states are weaker in this device likely caused by the larger unintentional twist angle introduced in the sample fabrication process.

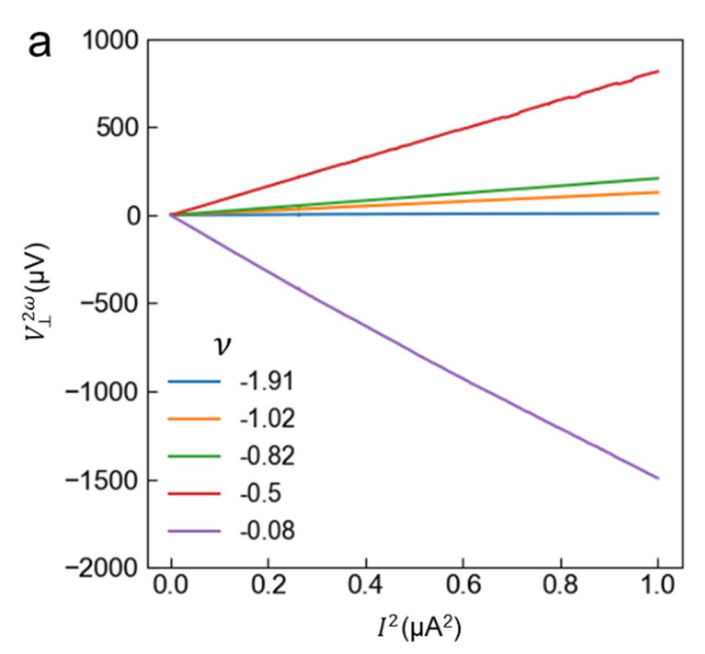


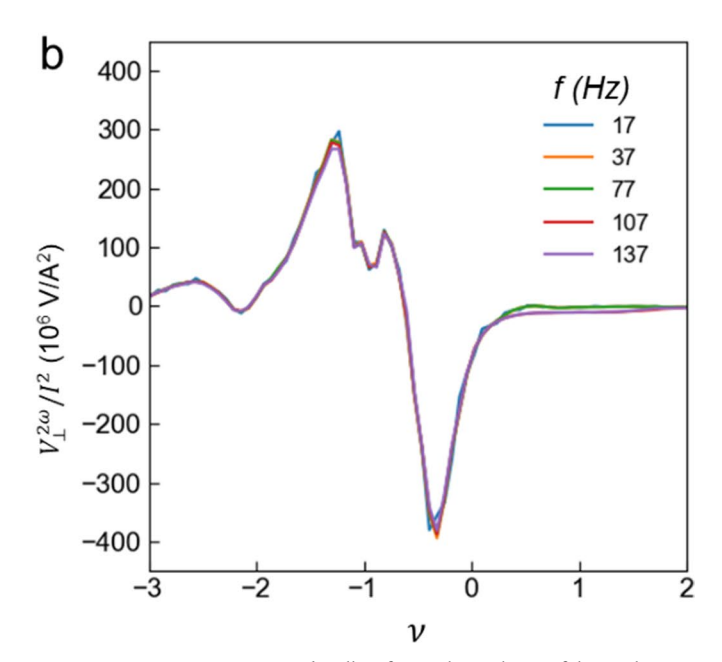
Extended Data Fig. 4 | Electric field dependent resistance at selected filling factors of ν =0,-1,-2. Arrows denote the electric field scan directions. The measurement temperature is 10 K. A clear hysteresis corresponding to

ferroelectric switching is observed. In addition to the ferroelectric switching, non-monotonic electric field dependence is also observed (see discussions in Methods).



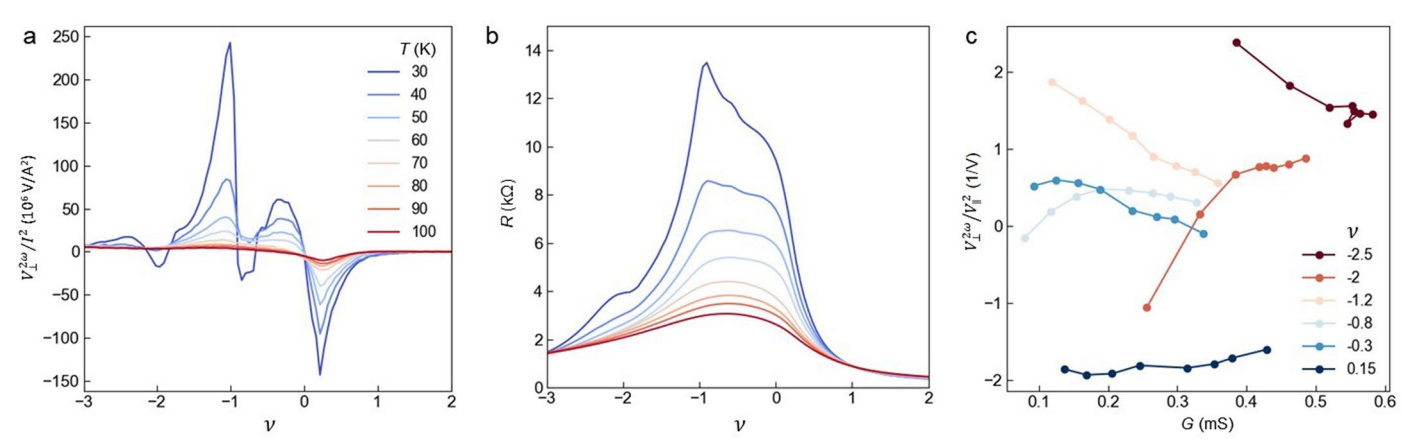
Extended Data Fig. 5 | **Variable-range hopping transport at different filling factors. a-d**, Resistance (in log scale) versus $T^{-1/2}$ for both P < 0 and P > 0 at v = 0 (**a**), -0.5 (**b**), -1.5 (**c**) and -2 (**d**). The linear dependence demonstrates the Efros-Shklovskii variable-range hopping.





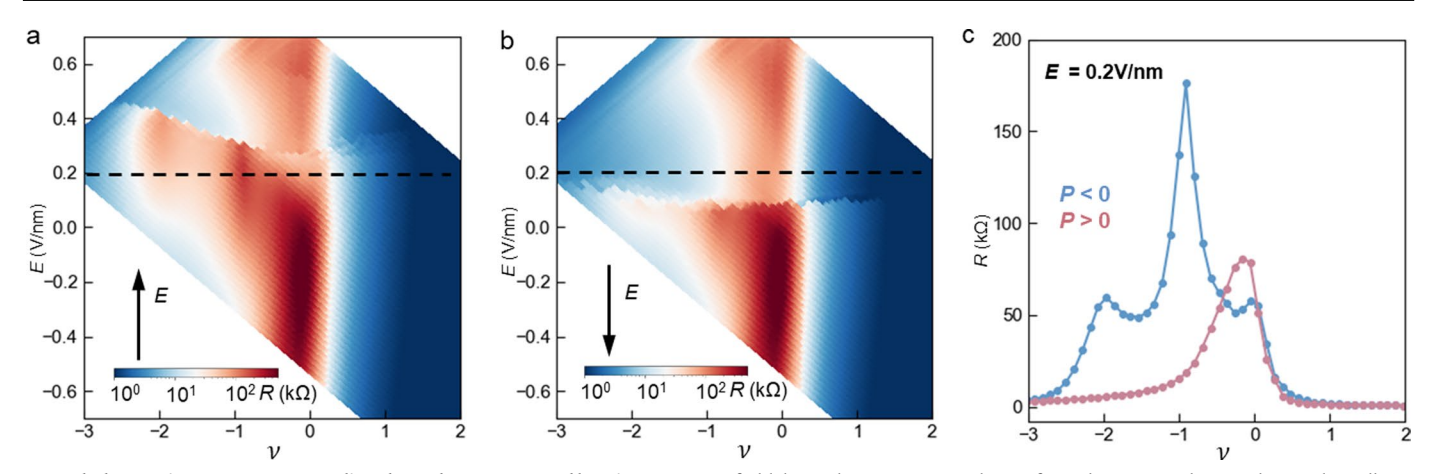
Extended Data Fig. 6 | Nonlinear anomalous Hall response. a, Linear dependence of the second-harmonic Hall voltage on the bias current squared at varying filling factors. The current modulation frequency is 17 Hz. The

measurement temperature is 25 K. **b**, Filling factor dependence of the nonlinear anomalous Hall response $V_{\perp}^{2\omega}/I^2$ at varying excitation frequencies of 17, 37, 77, 107, and 137 Hz. The response is independent of the excitation frequency.



Extended Data Fig. 7 | **Temperature dependent nonlinear anomalous Hall effect at** E**=0.2 V/nm and P<0. a**, **b**, Filling factor dependence of $\frac{V_1^{2\omega}}{L^2}$ (**a**) and the longitudinal resistance R (**b**) at varying temperatures from 30 K to 100 K. **c**, Extracted $V_1^{2\omega}/V_{\parallel}^2$ as a function of the sample conductance G at selected moiré filling factors from -2.5, to 0.15. Unlike the extrinsic NAHE in the coherent

metallic transport regime, in which $V_\perp^{2\omega}/V_\parallel^2 \propto G^2$ is expected and has been observed 26 , complicated dependence of $V_\perp^{2\omega}/V_\parallel^2$ on G is observed for the variable-range hopping transport regime here. Future studies are required to better understand the NAHE in the hopping transport regime.



Extended Data Fig. 8 | Transport studies along the WTe $_2$ crystal b-axis. a, b, Electric field and filling factor dependence for the longitudinal resistance of angle-aligned bilayer T $_d$ -WTe $_2$ /monolayer H-WSe $_2$ heterostructure at 10 K. The current is biased along the crystal b-axis of WTe $_2$ - The black arrows label the forward (a) and backward (b) electric field scan directions. Hysteretic electric

field dependence corresponding to ferroelectric switching is observed. **c**, Filling factor dependent longitudinal resistance extracted from **a** (blue) and **b** (red) at E = 0.2 V/nm (the black dashed lines in **a**, **b**). They denote the two spontaneous polarization states P > 0 and P < 0. Moiré insulating states are observed only for P < 0.